Stability of Al-Mn Transition Edge Sensors for Frequency Domain Multiplexing

J. Hubmayr, J. E. Austermann, J. A. Beall, D. Becker, D. A. Bennett, B. A. Benson, L. E. Bleem, C. L. Chang, J. E. Carlstrom, H.-M. Cho, A. T. Crites, M. Dobbs, W. Everett, E. M. George, W. L. Holzapfel, N. W. Halverson, J. W. Henning, G. C. Hilton, K. D. Irwin, D. Li, P. Lowell, M. Lueker, J. McMahon, J. Mehl, S. S. Meyer, J. P. Nibarger, M. D. Niemack, D. R. Schmidt, E. Shirokoff, S. M. Simon, K. W. Yoon, and E. Y. Young

***Abstract*—We are developing arrays of 150 GHz transition edge sensor (TES) polarimeters for the South Pole Telescope polarimeter (SPTpol). Prototype devices use an aluminum manganese (Al-Mn) alloy TES with a normal resistance R_n suited to frequency domain multiplexing (fMUX) used in SPTpol. Using the fMUX readout, the devices exhibit noise performance consistent with expectations when $\mathrm{R} > 0.8R_n$. Below $0.8R_n$, the detectors have high loopgain and become unstable, which is predicted by use of a compound TES model. We address this issue in a recent fabrication with increased TES heat capacity and normal metal structures on the TES to tune the temperature sensitivity.**

***Index Terms*—AlMn, CMB, polarimeter, transition edge sensor.**

I. Introduction

SCIENCE targets achievable through cosmic microwave background (CMB) polarimetry include observing signatures of inflation and measuring the sum of the neutrino masses. Achieving such goals requires instruments with high sensitivity and fine control over polarization systematic errors. To meet these demands, we are developing an all silicon focal plane composed of micro-machined silicon platelet feed-horn arrays [1], [2] coupled to monolithic arrays of transition edge sensor (TES) polarimeters for the South Pole Telescope polarimeter (SPTpol) [3]. SPTpol plans ~ 600 feed-horn coupled polarimeters operating near 150 GHz.

In these proceedings, we discuss the development of TES polarimeters suitable for frequency domain multiplexing (fMUX) [4], [5] used in SPTpol. Single pixel polarimeters with molybdenum copper (Mo:Cu) bilayer TESs used in time division multiplexing are well characterized [6]–[8]. We use the existing polarimeter design, substituting an Al-Mn film in place of the Mo:Cu bilayer, to obtain a normal resistance $R_n \sim 1\ \Omega$ matched for fMUX. We characterize the device thermal conductivity and temperature sensitivity using fMUX. The onset of electro-thermal oscillations are observed when operating the TES at modest depths into the superconducting transition, which is predicted by use of a compound TES model. This instability limits the operating range of the sensor to above $0.8R_n$, decreasing the sensor dynamic range. We address this issue in our second round of fabrication by increasing the effective TES heat capacity with additional metal thermally connected to the TES [9] as well as by tuning the TES temperature sensitivity with normal metal structures on the Al-Mn film [10], [11].

II. Polarimeter Design

Fig. 1 shows a photograph of the 6 mm SPTpol test pixel fabricated at the National Institute of Standards and Technology. The corrugated feed-horn (not shown) transitions to a 1.6 mm circular waveguide for operation at 145 GHz. Four Nb probes inside the circular waveguide comprise the orthomode transducer (OMT), which launches radiation in X and Y polarizations onto separate superconducting circuits. The power in X and Y is deposited on separate thermally isolated membranes and sensed with transition edge sensors (TESs). Details of the pixel design are described in [12] and [13].

The $305 \times 300\ \mu\mathrm{m}$ island contains a lossy Au meander that deposits the power from the superconducting circuit onto the island. This power is sensed with a 1200 ppm by atomic percent Al-Mn TES [14], [15] with dimensions $0.05 \times 48 \times 92\ \mu\mathrm{m}^3$. The $0.05 \times 48 \times 68\ \mu\mathrm{m}^3$ active area has $R_n \sim 0.9\ \Omega$ and $T_c \sim 525\ \mathrm{mK}$. The calculated heat capacity of the Al-Mn TES is 25.6 fJ/K, assuming bulk aluminum and half the BCS enhancement [16]. The island also contains a $\sim 2\ \Omega$ Au heater for sensor calibration. The membrane island is thermally isolated and suspended by four $\mathrm{SiN}/\mathrm{SiO}_x$ legs with dimensions $0.5/0.45 \times 9 \times 350\ \mu\mathrm{m}^3$.

Manuscript received August 03, 2010. Date of publication December 03, 2010; date of current version May 27, 2011. Work at the University of Chicago is supported by the NSF through grant ANT-0638937 and NSF Frontier Center grant PHY-0114422 to KICP at the University of Chicago. Generous support also received from the Kalvi Foundation and the Gordon and Betty Moore Foundation.

J. Hubmayr, J. A. Beall, D. Becker, D. A. Bennett, H.-M. Cho, G. C. Hilton, K. D. Irwin, D. Li, P. Lowell, J. P. Nibarger, M. D. Niemack, D. R. Schmidt, and K. W. Yoon are with the NIST Quantum Devices Group, Boulder, CO 80305 USA.

J. E. Austermann, N. W. Halverson, J. W. Henning, and S. M. Simon are with the Center for Astrophysics and Space Astronomy, Department of Astrophysical and Planetary Sciences and Department of Physics, University of Colorado, Boulder, CO 80309 USA.

B. A. Benson, L. E. Bleem, C. L. Chang, J. E. Carlstrom, A. T. Crites, W. Everett, J. Mehl, and S. S. Meyer are with the Kavli Institute for Cosmological Physics, University of Chicago, Chicago, IL 60637 USA.

M. Dobbs is with the Department of Physics, McGill University, Montreal, Quebec, H3A 2T8, Canada.

E. M. George, W. L. Holzapfel, M. Lueker, E. Shirokoff, and E. Y. Young are with the Department of Physics, University of California, Berkeley, CA 94720 USA.

J. McMahon is with the Department of Physics, University of Michigan, Ann Arbor, MI 48109 USA.

Color versions of one or more of the figures in this paper are available online at http://ieeexplore.ieee.org.

Digital Object Identifier 10.1109/TASC.2010.2090630

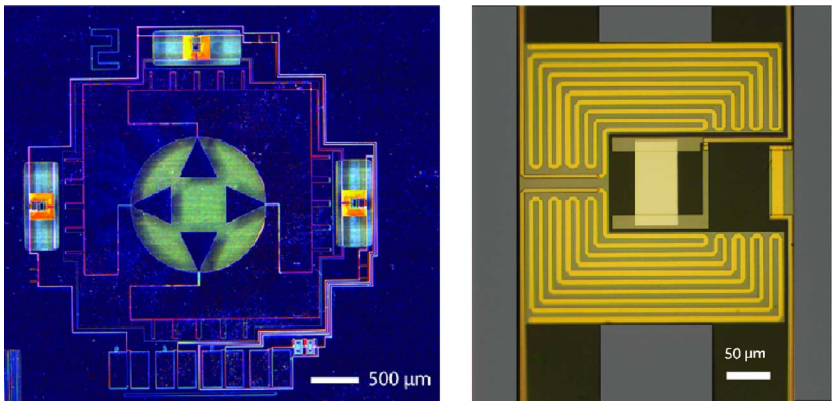

Fig. 1. (Left) Optical micrograph of the prototype polarimeter. Nb OMT fins couple X [Y] polarized light onto the isolated membranes located on the top (right side). A dark TES used for systematic error checks is located on the left. (Right) Enlargement of the thermally isolated TES island. The Al-Mn TES is located in the center. Au meander surrounds the TES, and the Au heater is located on the right.

III. Detector Characterization

To determine the properties of the devices, we operate the detectors dark, inside a black enclosure heat-sunk to the base plate of a ^{3}He adsorption refrigerator capable of cooling to 270 mK. We place an LC resonant filter with $L = 16\ \mu$H and $450 < \nu_o < 500$ kHz in series with the TES. Current is read out by a series array SQUID amplifier [17] mounted at 4 K. Digital frequency domain multiplexing (DfMUX) electronics [18] AC biases the TES on the LC resonance and demodulates the SQUID response.

The two devices tested show similar performance. We report the results from device TES163D, a dark TES.

A. Thermal Conductance

To determine the power flow across the thermal link, we measure TES current versus voltage (IV) curves as a function of bath temperature T_{bath}. Fig. 2 shows the measured Joule power P evaluated at 0.9, 0.8 and $0.7R_n$ as a function of bath temperature including fits assuming

$$P = K\left(T^n - T_{bath}^n\right). \tag{1}$$

Here T is the temperature of the thermally isolated membrane. The best fit parameters are $K = 103$ pW/K^n, n $= 2.55$ and $T_c = 523.7$ mK with variation of the parameters $< 0.5\%$ between the three fits. Because of the agreement between the fits as a function of R_n fraction, we need not let n and K be functions of resistance in determining the TES temperature discussed below. From the best fit parameters $G \equiv dP/dT = 96.4$ pW/K.

B. TES Transition

By use of the fit parameters of (1), a power axis from an IV curve can be converted to TES temperature. With this conversion, we map the transition $R(T)$ as well as the "IV loopgain" $(\mathcal{L}_{iv}(R) \equiv P\alpha_{iv}/GT)$ for several bath temperatures in Fig. 3. Like any feedback system, the loopgain is an important parameter that quantifies the strength of feedback and influences stability. Here $\alpha_{iv} \equiv \partial \ln R/\partial \ln T$, where R and T are determined from IV curves. The distinction between α_{iv} and α commonly reported in the literature is that the resistance is not determined at constant current in α_{iv}. The two quantities, as well as $\mathcal{L}$ and $\mathcal{L}_{iv}$, are equivalent when the resistance is independent of current [19], that is when $\beta \equiv \partial \ln R/\partial \ln I|_{T_o} = 0$.

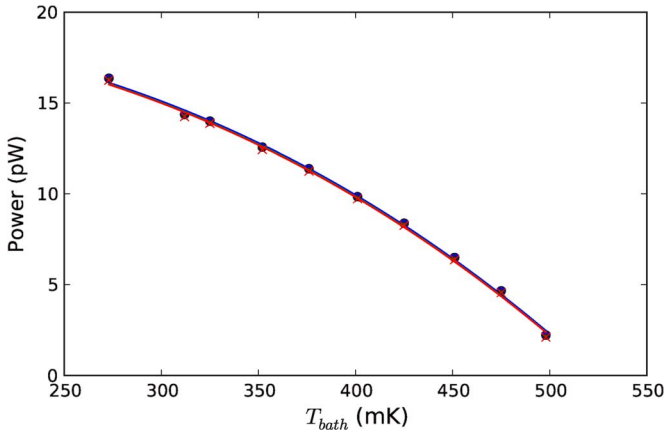

Fig. 2. Electrical power evaluated at (points) 0.9, 0.8, and $0.7R_n$ versus bath temperature together with (lines) fits to (1). The measurements and fits for different R_n fractions cannot be distinguished on the scale of this plot.

C. Thermal Response

To probe the thermal circuit of the TES island, we perform the measurement described by Lueker [20] using the DfMUX electronics. After biasing the bolometer into the transition, a small test signal voltage sweeps in frequency, providing a fluctuating input power. By use of a lock-in technique, the current response to the purely thermal signal is recorded. This measurement determines the magnitude of the normalized current responsivity $|s_I(\nu)/s_I(0)|$, where $s_I \equiv dI/dP$. Fig. 4 shows the result of this measurement for several bias positions.

The responsivity curves of Fig. 4 do not fit a simple one-pole TES model. The inflection point near 2 kHz at 0.85 Ω shows that the TES thermally decouples from the isolated membrane. At the two lowest bias points, the increased response at 20 kHz is evidence of interaction between two poles. The sharp cut-off above 20 kHz is due to the LC filter.

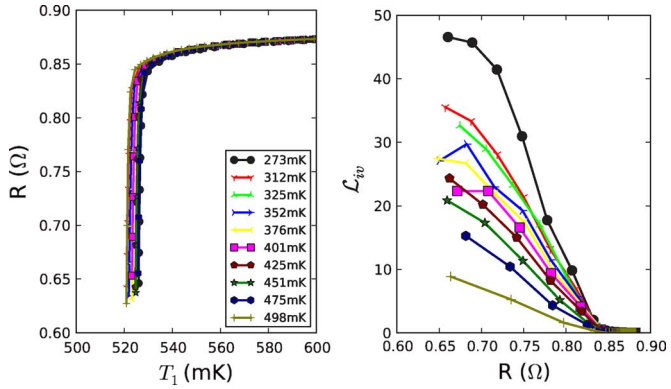

Fig. 3. Resistance versus temperature and IV loopgain ($\mathcal{L}_{iv}$) versus resistance for several bath temperatures.

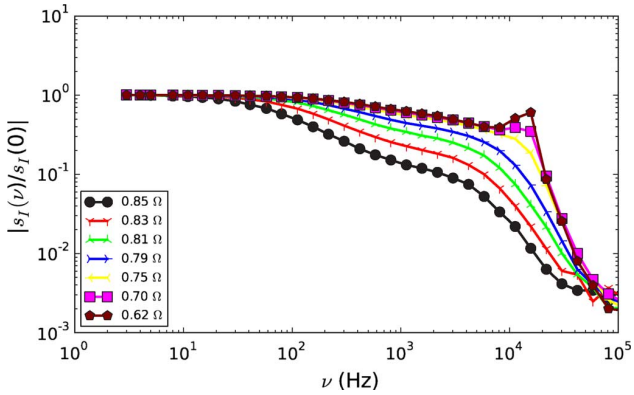

Fig. 4. Normalized responsivity measurement using the technique described in [20] for several bias points in the transition.

D. Noise and Stability

We measure white noise levels of $4.4 \times 10^{-17}\ \mathrm{W}/\sqrt{\mathrm{Hz}}$ near the expected noise level when biased to $0.9R_n$ and $T_{bath} = 270\ \mathrm{mK}$. However, when the bolometer is biased below $0.8R_n$, we find excess noise and observe spontaneous thermal oscillations. These bound electro-thermal oscillations [20] render the TES unusable at these bias points and thereby decrease the available dynamic range.

IV. Bolometer Thermal Model

In an effort to understand the observed instability of the device, we model the electro-thermal circuit and use the measurements reported in the previous section as input parameters to the model. The thermal response curves of Fig. 4 motivate a model beyond the simple TES described by Irwin and Hilton [21]. Moreover, the simple TES model does not predict the observed instability below $0.8R_n$ based on input parameters determined from measurements in the previous section. Recently, Bennett *et al.* developed a time domain analytic model of the compound TES in the small-signal limit [22]. We use this lumped-element model shown in Fig. 5 to predict the stability of our TES.

Bennett's model assumes a DC bias circuit. Because our TES is operated under AC bias, we convert to an equivalent DC bias circuit by substituting $2L$ in place of the series LC. This substitution is valid when biased near the LC resonance. In addition to the parameters defined in Fig. 5, the model includes the

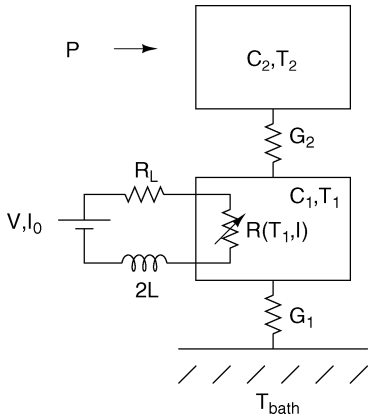

Fig. 5. Lumped-element electro-thermal model of the compound TES. C_1 (C_2) is the heat capacity of the TES (absorber). The differential thermal conductance between the bodies is described by G_1 and G_2. We represent the TES by $R(T_1, I)$ with a steady-state resistance R_o. The TES is biased with a voltage source and equivalent load resistor R_L that produces a steady-state current I_o. The TES is placed in series with an inductor $2L$, which accounts for the decreased bandwidth under AC bias as compared to DC.

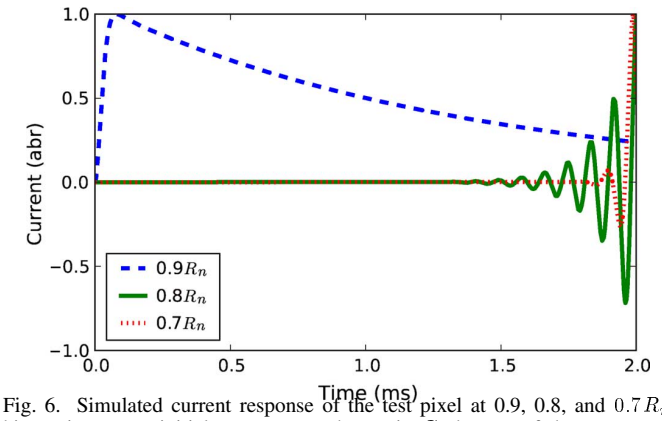

Fig. 6. Simulated current response of the test pixel at 0.9, 0.8, and $0.7R_n$ bias points to an initial temperature change in C_2 by use of the compound TES model. The parameter values shared among the three models are $C_1 = 25.6\ \mathrm{fW/K}$, $C_2 = 1\ \mathrm{pJ/K}$, $G_1 = 96.4\ \mathrm{pW/K}$, $G_2 = 2700\ \mathrm{pW/K}$, $R_L = 0.03\ \Omega$, $2L = 32\ \mu\mathrm{H}$, and $\beta = 0$. The resistance and loopgain at 0.9, 0.8, and $0.7R_n$ are $R_o = 0.81$, 0.72, and 0.63 Ω, and $\mathcal{L} = 10$, 40, 50, respectively. The curves are normalized to maximum current.

TES temperature sensitivity $\alpha \equiv \partial \ln R/\partial \ln T|_{I_o}$ and current sensitivity $\beta \equiv \partial \ln R/\partial \ln I|_{T_o}$, evaluated at constant current and temperature, respectively. We associate C_1 with the heat capacity of the Al-Mn TES and C_2 with the summed heat capacity of the remaining elements on the isolated membrane.

The current response of the compound TES to an initial temperature change ΔT in the absorber C_2 is

$$\delta I(t) = \frac{\Delta T \mathcal{L} G_1 G_2}{I_o L C_1} \left(A_1 e^{t/\tau_1} + A_2 e^{t/\tau_2} + A_3 e^{t/\tau_3} \right). \quad (2)$$

Here $A_{1,2,3}$ are the amplitudes determined by initial conditions and $\tau_{1,2,3}$ govern the time evolution of the current. The time constants are a non-trivial function of all 11 parameters in the model. Instability occurs when $\Re(\tau_{1,2,3}) > 0$. In this case the current increases over time to the initial temperature change. For further details of the model see [22].

By use of (2), Fig. 6 shows the simulated current response to an initial temperature change in the absorber with the TES biased to 0.9, 0.8 and $0.7R_n$. The input parameters to the model

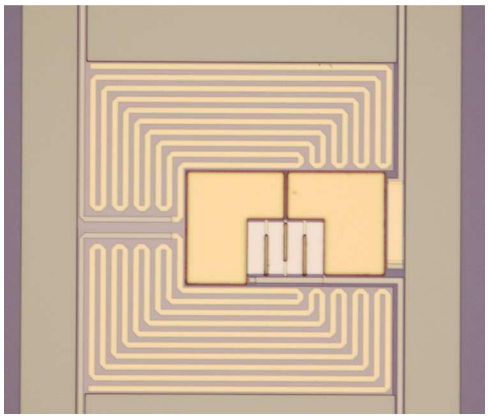

Fig. 7. Example of a second-generation TES island that includes added TES heat capacity with Au (surrounding the Al-Mn film) and lines of normal metal dots on the Al-Mn film.

include the bolometer parameters determined from the measurements in Section III (R_o, G_1, T_c and $\mathcal{L}(R_o)$ assuming $\beta = 0$), G_2 and C_2 from complex impedance measurements of the Mo:Cu devices in [6] and the calculated value of the TES heat capacity (C_1). While the current response at $0.9R_n$ relaxes back to steady-state, the responses at both $0.8R_n$ and $0.7R_n$ show growing oscillations. If we allow $\beta \neq 0$ while fixing R_o and $\mathcal{L}$, we find that the TES exhibits damped oscillations at $0.7R_n$ bias if $\beta > 2.8$. Since we operate the detector high in the transition, we do not expect $\beta \gtrsim 1$.

V. Discussion

The two-body thermal model suggests that the source of instability is insufficient thermal coupling of the Al-Mn film to the isolated membrane island when the TES is operated in strong electro-thermal feedback [23]. Gains in stability can be made either by improving the thermal connection between membrane and TES or by slowing down the TES. In CMB experiments, the detector time constant need not be lower than a few times the scan speed of the telescope (typically $\tau_{sensor} \sim 1$ ms). With a peak $\mathcal{L} = 40$, we can easily meet this requirement. However, in order to extend the dynamic range, we would like to decrease α slightly so that the same loopgain is reached deeper in transition.

The second generation of test devices (see Fig. 7) includes several geometry to explore the thermal connection between TES and membrane and includes two measures to slow the response of the TES. These measures are added heat capacity in Au or PdAu thermally connected to the TES and normal metal structures on the Al-Mn TES to tune α. Preliminary measurements of these devices show stability below $0.3R_n$. The current study of the second generation detectors will be used to optimize a final design.

VI. Conclusion

Prototype, 150 GHz SPTpol detectors with Al-Mn films have high temperature sensitivity and expected noise performance high in the superconducting transition as read out with frequency domain multiplexing electronics. However, the devices are unstable when operated below $\sim 0.8R_n$ for which the loopgain $\mathcal{L}$ exceeds 40. This behavior is predicted by use of a compound TES model. The second-generation TES islands address this issue through increased TES heat capacity with Au and PdAu contacting the Al-Mn film in several geometry, as well as normal-metal structures on the Al-Mn film to tune the temperature sensitivity.

References

[1] J. W. Britton *et al.*, "Corrugated Silicon Platelet Feed Horn Array for CMB Polarimetry at 150 GHz," *SPIE Astro. Inst.*, vol. 7741, 2010.

[2] J. W. Britton *et al.*, "Corrugated feedhorn arrays in Silicon," *LTD 13*, vol. 1185, pp. 375–378, 2009.

[3] J. J. McMahon *et al.*, "SPTpol: an instrument for CMB polarization," *LTD 13*, vol. 1185, pp. 511–514, 2009.

[4] T. M. Lanting *et al.*, "Frequency-domain multiplexed readout of transition-edge sensor arrays with a superconducting quantum interference device," *Appl. Phys. Lett.*, vol. 86, pp. 112511–112513, 2005.

[5] T. M. Lanting *et al.*, "A frequency-Domain SQUID multiplexer readout for arrays of transition-edge sensors," *IEEE Trans. Appl. Supercond.*, vol. 13, no. 2, pp. 626–629, 2003.

[6] J. W. Appel *et al.*, "Characterizing and modeling the noise and complex impedance in feedhorn-coupled TES polarimeters," *LTD 13*, vol. 1185, pp. 211–214, 2009.

[7] J. E. Austermann *et al.*, "Measurements of bolometer uniformity for feedhorn coupled TES polarimeters," *LTD 13*, vol. 1185, pp. 498–501, 2009.

[8] L. E. Bleem *et al.*, "Optical properties of Feedhorn-coupled TES polarimeters for CMB polarimetry," *LTD 13*, vol. 1185, pp. 479–482, 2009.

[9] E. Shirokoff *et al.*, "The South Pole Telescope SZ-receiver detectors," *IEEE Trans. Appl. Supercond.*, vol. 19, pp. 517–519, 2009.

[10] J. N. Ullom, "Suppression of excess noise in Transition-Edge Sensors using magnetic field and geometry," *Nucl. Instrum. Methods Phys. Res. A*, vol. 520, pp. 333–335, 2004.

[11] J. G. Staguhn *et al.*, "Approaching the fundamental noise limit in Mo/Au TES bolometers with transverse normal metal bars," *Nucl. Instrum. Methods Phys. Res. A*, vol. 520, pp. 336–339, 2004.

[12] K. W. Yoon *et al.*, "Feedhorn-Coupled TES polarimeters for next-generation CMB instruments," *LTD 13*, vol. 1185, pp. 515–518, 2009.

[13] J. J. McMahon *et al.*, "Planar orthomode transducers for feedhorn-coupled TES polarimeters," *LTD 13*, vol. 1185, pp. 490–493, 2009.

[14] S. W. Deiker *et al.*, "Superconducting transition edge sensor using dilute AlMn alloys," *Appl. Phys. Lett.*, vol. 85, p. 2137, 2004.

[15] D. R. Schmidt *et al.*, "Al-Mn transition edge sensors for CMB polarimeters," *IEEE Trans. Appl. Supercond.*, 2010.

[16] J. Bardeen, L. N. Cooper, and J. R. Schreiffer, "Theory of superconductivity," *Phys. Rev.*, vol. 108, no. 5, pp. 1175–1204, 1957.

[17] M. E. Huber *et al.*, "DC SQUID series array amplifiers with 120 MHz bandwidth," *IEEE Trans. Appl. Supercond.*, vol. 11, pp. 1251–1256, 2001.

[18] M. Dobbs, E. Bissonnette, and H. Spieler, "Digital frequency domain multiplexer for mm-wavelength telescopes," *IEEE Trans. Nucl. Sci.*, vol. 55, pp. 21–26, 2008.

[19] S. J. Smith *et al.*, "Characterizing the superconducting-to-normal transition in Mo/Au transition-edge sensor bilayers," *J Low Temp. Phys.*, vol. 151, p. 195200, 2008.

[20] M. Lueker *et al.*, "Thermal design and characterization of transition-edge sensor (TES) bolometers for frequency-domain multiplexing," *IEEE Trans. Appl. Supercond.*, vol. 19, pp. 496–500, 2009.

[21] K. D. Irwin and G. C. Hilton, "Transition-edge sensors," *Cryogenic Particle Detection Topics Appl. Phys.*, vol. 99, pp. 63–149, 2005.

[22] D. A. Bennett, "An analytical model for pulse shape and electrothermal stability in two-body microcalorimeters," *Appl. Phys. Lett.*, vol. 97, p. 102504, 2010.

[23] K. D. Irwin, "An application of electrothermal feedback for high resolution cryogenic particle detection," *Appl. Phys. Lett.*, vol. 60, no. 15, pp. 1998–2000, 1995.